Journal of Solid State Chemistry 184 (2011) 3128–3133

Contents lists available at SciVerse ScienceDirect

Journal of Solid State Chemistry

journal homepage: www.elsevier.com/locate/jssc

Low-temperature structural phase transition in synthetic libethenite Cu_2PO_4OH

Alexei A. Belik [a,*], Panče Naumov [b], Jungeun Kim [c], Shunsuke Tsuda [d]

[a] International Center for Materials Nanoarchitectonics (MANA), National Institute for Materials Science (NIMS), 1-1 Namiki, Tsukuba, Ibaraki 305-0044, Japan
[b] Department of Material and Life Science, Graduate School of Engineering, Osaka University, 2-1 Yamada-oka, Suita, Osaka 565-0871, Japan
[c] Japan Synchroron Radiation Research Institute (JASRI), 1-1-1 Kouto, Sayo-cho, Hyogo 679-5198, Japan
[d] Superconducting Properties Unit, National Institute for Materials Science (NIMS), 1-2-1 Sengen, Tsukuba, Ibaraki 305-0047, Japan

ARTICLE INFO

Article history:
Received 19 May 2011
Received in revised form
1 August 2011
Accepted 22 September 2011
Available online 29 September 2011

Keywords:
Adamite family
Mineral libethenite
Crystal structure
Single crystal
Specific heat

ABSTRACT

Low-temperature structural properties of the synthetic mineral libethenite Cu_2PO_4OH were investigated by single-crystal X-ray diffraction, synchrotron X-ray powder diffraction, specific heat measurements, and Raman spectroscopy. A second-order structural phase transition from the *Pnnm* symmetry ($a=8.0553(8)$ Å, $b=8.3750(9)$ Å, $c=5.8818(6)$ Å at 180 K) to the $P2_1/n$ symmetry ($a=8.0545(8)$ Å, $b=8.3622(9)$ Å, $c=5.8755(6)$ Å, $\beta=90.0012(15)$ at 120 K) was found at 160 K during cooling. At 120 K, the monoclinic angle is 90.0012(15) from single crystal X-ray data vs 90.083(1) from powder X-ray diffraction data. The $P2_1/n$–to–*Pnnm* transition may be a general feature of the adamite-type compounds, M_2XO_4OH.

1. Introduction

The synthetic mineral libethenite, Cu_2PO_4OH [1,2], has attracted attention recently as a photocatalyst for reactions with visible light [3–6]. The morphological [7], structural [8–11], optical [1], and vibrational [12–14] properties of libethenite have also been investigated. Cu_2PO_4OH belongs to a family of adamite-type compounds, M_2XO_4OH [1,2]. The mineral adamite, Zn_2AsO_4OH, crystallizes in space group *Pnnm* with $a=8.306$, $b=8.524$, and $c=6.043$ Å [1]. A number of minerals have identical or related structures [1,2], e.g., libethenite, eveite Mn_2AsO_4OH, zincolibethenite $CuZnPO_4OH$ [15], tarbuttite Zn_2PO_4OH, and paradamite Zn_2AsO_4OH. The mineral olivenite Cu_2AsO_4OH has a monoclinically distorted structure at room temperature (space group $P2_1/n$; $\beta=90.0^\circ$ from single-crystal data and 90.08° from powder diffraction data) [16]. Synthetic compounds Co_2PO_4OH and Co_2AsO_4OH demonstrate interesting magnetic properties: spin-glass behavior in a three-dimensional antiferromagnetically-ordered phase for Co_2PO_4OH [17] and a sinusoidal magnetic structure for Co_2AsO_4OH [18,19]. A variety of substitution effects have been studied in both Co_2PO_4OH and Co_2AsO_4OH [20–26].

Detailed magnetic properties of Cu_2PO_4OH have recently been investigated by spin-dimer analysis, magnetic susceptibility, high-field magnetization, specific heat, and NMR [27,28]. Cu_2PO_4OH has a spin gap arising from the presence of square-tetramer cluster units [27,29]. The entire order of solid solutions $Co_{2-x}Cu_xPO_4OH$ ($0\le x\le 2$) was also investigated by magnetic susceptibility, specific heat, and neutron powder diffraction [21]. During the course of our investigation of Cu_2PO_4OH, we observed a structural phase transition in this compound at 160 K that appears to have been overlooked in all previous works. Structural studies on Cu_2PO_4OH have been performed above room temperature, and no phase transitions were found [11]. In this work, we report on the structural properties of synthetic libethenite Cu_2PO_4OH at low temperature.

2. Experimental section

Synthesis of single crystals of Cu_2PO_4OH is described in our previous work [27]. Synchrotron powder X-ray diffraction (XRD) data of crashed crystals of Cu_2PO_4OH were measured on a large Debye–Scherrer camera at the BL02B2 beamline of SPring-8 [30] between 90 and 300 K. The incident beam from a bending magnet was monochromatized to $\lambda=0.4227$ Å. The sample was packed in a glass capillary tube with an inner diameter of 0.3 mm, and the capillary was rotated during the measurements. The synchrotron powder XRD data were collected in a 2θ range from 2° to 75° with a step interval of 0.01°, and the data were analyzed with RIETAN 2000 [31]. The cooling was performed using an N_2 gas flow system. The sample was first cooled to 90 K, and the

* Corresponding author.
E-mail address: alexei.belik@nims.go.jp (A.A. Belik).

0022-4596/$ - see front matter © 2011 Elsevier Inc. All rights reserved.
doi:10.1016/j.jssc.2011.09.026

measurements were performed on heating. At some intermediate temperatures, crystallization of ice that occasionally occurred on the capillary tube became apparent, which was removed by the gas stream at higher temperatures.

For the single-crystal X-ray data collection at 180 K and 120 K (the temperatures are uncorrected), the same emerald green crystalline block ($200 \times 180 \times 175$ μm), from which the structure at 200 K had been refined previously [27], was used in this study. At either temperature, 1900 frames of 0.3° width were collected on a three-circle Bruker SMART APEX diffractometer equipped with CCD detector [32] by sequential exposures during 30 s of the crystal to monochromatic Mo $K\alpha$ X-rays ($\lambda = 0.71073$ Å). The reflection data were merged and integrated using SAINT [32].

Specific heat, $C_p(T)$, of Cu_2PO_4OH was measured between 300 and 1.8 K on cooling and heating at a zero magnetic field by a pulse relaxation method using a commercial calorimeter (Quantum Design PPMS). The $C_p(T)$ data were measured using one single crystal weighing about 3 mg. No visible damage could be detected on this single crystal after cooling to 1.8 K, and the crystal retained its shape and transparency. Magnetic susceptibilities, $\chi = M/H$, were measured on a SQUID magnetometer (Quantum Design, MPMS) between 2 and 400 K in fields of 100 Oe, 1 kOe, and 10 kOe under both zero-field-cooled (ZFC) and field-cooled (FC; on cooling) conditions. No field dependence of the magnetic susceptibilities was observed.

The Raman spectra were recorded using a 64-cm-long single monochromator (Photon Design Co., PDPX) with a low-pass filter to discriminate the Raman signal from the excitation laser light (514.5 nm). The excitation power was set to less than 3 mW to avoid radiation damage. The sample temperature was controlled by a commercially available liquid nitrogen cryostat (Linkam Scientific Instruments, THMS600). The Raman spectra between 30 and 750 cm^{-1} were collected from 100 K to 180 K with a step of 10 K.

3. Results and discussion

Fig. 1 shows fragments of the synchrotron powder XRD data between 100 and 280 K. Above 170 K, all reflections could be indexed with the lattice parameters of $a \approx 8.055$ Å, $b \approx 8.375$ Å, $c \approx 5.882$ Å and the space group *Pnnm*, in agreement with the single-crystal structural data above 200 K [8–10,27]. The reflection conditions of *Pnnm* are $k+l=2n$ for 0*kl*, $h+l=2n$ for *h*0*l*, $h=2n$ for *h*00, $k=2n$ for 0*k*0, and $l=2n$ for 00*l* [33]. New reflections appeared below 160 K with indexes 0*kl* and $k=2n+1$ and $l=2n+1$ (Fig. 1). The new reflection conditions ($h+l=2n$ for *h*0*l*, $h=2n$ for *h*00, $k=2n$ for 0*k*0, and $l=2n$ for 00*l*) suggest only one possible space group $P2_1/n$ [33] (no orthorhombic space groups satisfy these conditions). Nevertheless, in order to check the possibility of overlap of some reflections with others or eventual weak intensities in the powder XRD patterns we checked different orthorhombic subgroups of *Pnnm* in the Rietveld analyses. Table 1 shows that the *R* values were comparable for the *Pnnm* and $P2_1/n$ models at 280 K (the $P2_1/n$ model has larger number of refined structural parameters resulting in slightly smaller *R* values). At 100 K, orthorhombic structural models gave noticeably larger *R* values compared with the $P2_1/n$ model. In addition, the orthorhombic models could not fit well the 0*kl* reflections. Fig. 2 shows fragments of the Rietveld refinement fits for different models at 100 K and 280 K. The temperature dependences of the monoclinic angle (β) and the unit cell volume (V) are given in Fig. 3. The monoclinic angle gradually increases with decreasing temperature below 160 K. There was no step-like anomaly in the temperature dependence of the unit cell volume, indicating that this transition is probably of the second order.

Table 1
R values of the Rietveld refinements for different structural models of libethenite at 280 K and at 100 K.

Temperature (K)	Structural model	R_{wp} (%)	R_p (%)	R_I (%)
280	*Pnnm*	4.28	3.21	1.98
280	$P2_1/n$, $\beta=90°$ fixed	4.18	3.14	1.91
280	$P2_1/n$, $\beta=90.001(3)°$	4.20	3.15	1.92
100	*Pnnm*	6.45	4.77	2.17
100	$Pmn2_1$	6.35	4.71	2.12
100	$P2_1/n$, $\beta=90°$ fixed	5.99	4.41	1.91
100	$P2_1/n$, $\beta=90.098(1)°$	3.92	2.92	1.83

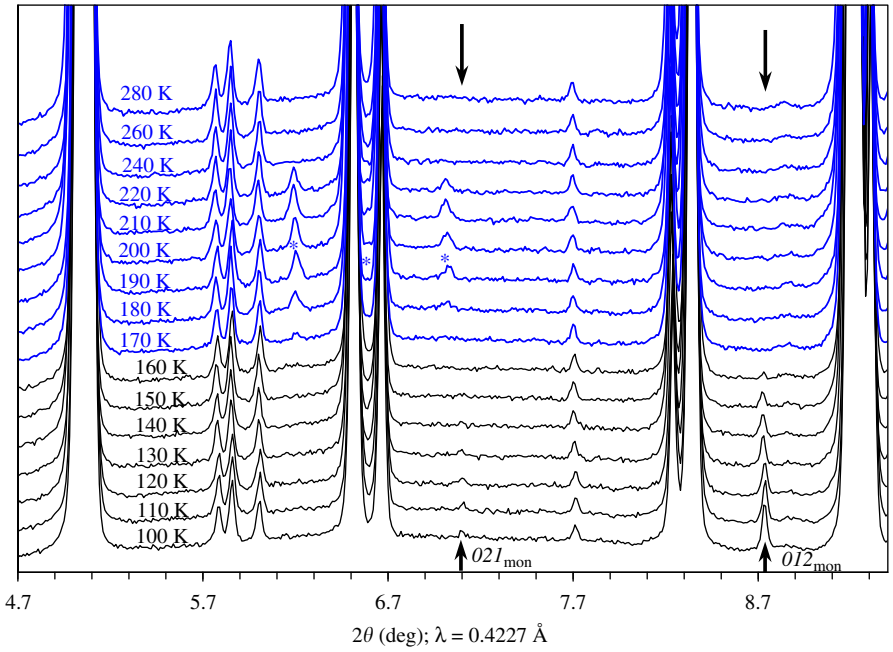

Fig. 1. Fragments of experimental synchrotron ($\lambda = 0.4227$ Å) X-ray powder diffraction patterns of Cu_2PO_4OH between 100 and 280 K. Arrows show additional reflections that appear below 160 K in the monoclinic $P2_1/n$ phase (indexes of these reflections are given). The reflections marked with asterisks are artefacts from ice (ICDD Card 85-1395), which appears occasionally on a capillary tube during the cooling by an N_2 gas flow system; the cooling system was also responsible for blowing off the ice.

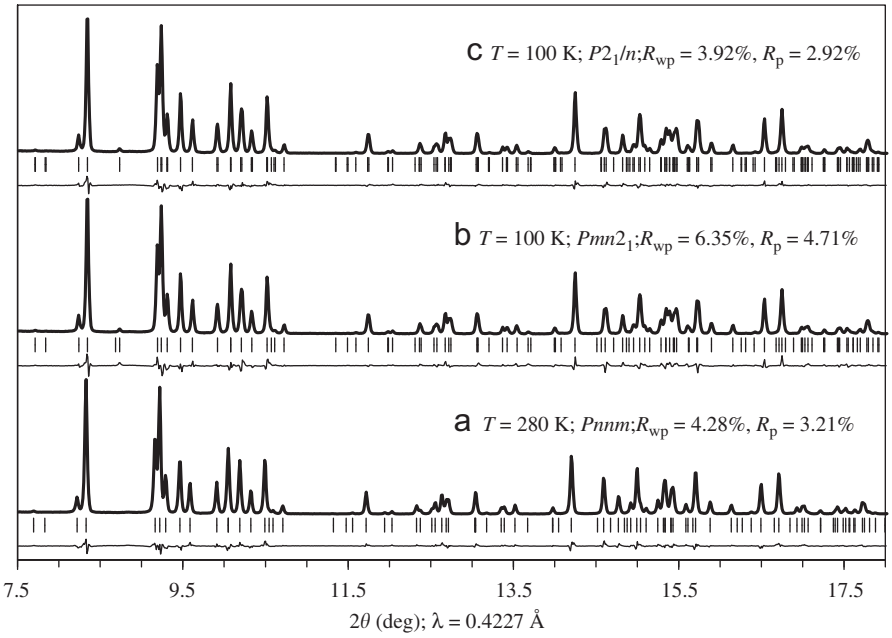

Fig. 2. Portions of the experimental and difference synchrotron (λ=0.4227 Å) X-ray powder diffraction patterns of Cu_2PO_4OH at (a) 280 K in the *Pnnm* model, (b) 100 K in the $Pmn2_1$ model, and (c) 100 K in the $P2_1/n$ model. The Bragg reflections are indicated by tick marks, and *R* values are given.

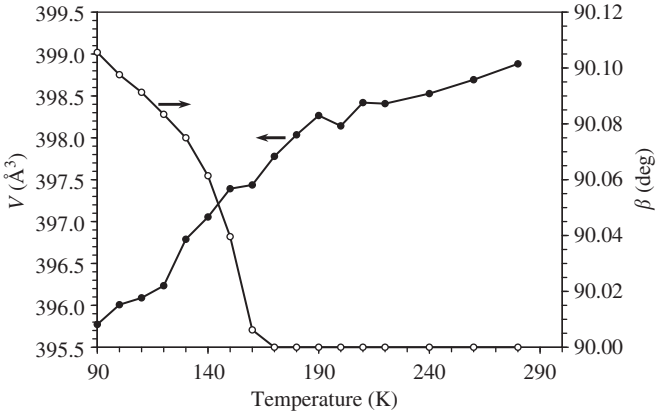

Fig. 3. Temperature dependence of the monoclinic angle, β (the error bars are smaller than the circle symbols), and the unit cell volume, *V*, in Cu_2PO_4OH. Above 170 K, the monoclinic angle was fixed at 90°.

Specific heat measurements showed a clear anomaly at 160 K (Fig. 4), confirming the existence of a phase transition. No difference was observed between the cooling and heating curves. This observation confirms the second order of the phase transition. On the other hand, no anomalies were observed in the magnetic susceptibilities at the phase transition point [27]. The inset of Fig. 4 shows the $d\chi/dT$ vs *T* curve intended to illustrate the absence of anomaly near 160 K.

The Raman spectra at 100 K and 180 K are shown in Fig. 5 (detailed data are provided as Supplementary material). Below 160 K, new weak modes appeared at 115 and 325 cm^{-1} and some phonon modes (at 140 cm^{-1}, 160 cm^{-1}, and 170 cm^{-1}) became noticeably sharper.

The structure at 180 K determined from single crystal corresponds to the orthorhombic *Pnnm* room-temperature phase. It was refined to R_1=2.73% by assigning anisotropic displacement parameters to all non-H atoms. The H-atom was positioned in the difference map and refined without constraints. The final cell parameters at 180 K are: a=8.0553(8) Å, b=8.3750(9) Å, c=5.8818(6) Å, $\alpha=\beta=\gamma=90°$, V=396.80(7) $Å^3$, Z=4, ρ_{calc}=4.002 g cm^{-3}, μ=11.021 mm^{-1}, $F(0\,0\,0)$=456. The details of data collections and refinements are given in Table 2. The structure parameters are given in Table 3 and the bond lengths are listed in Table 4.

Contrary to the room-temperature phase, the 0*kl* reflections of the initial cell at 120 K (a'=5.87, b'=8.05, c'=8.36 Å) for odd $k+l$ were present, clearly indicating monoclinic $P2_1/n$ symmetry. The data were corrected for absorption effects with SADABS [32]. For reasons of structural comparison with the high-temperature phase, the cell was transformed to a=8.05, b=8.36, and c=5.87 Å. A very small deviation from the orthorhombic symmetry, which was also observed in the room-temperature structure of olivenite Cu_2AsO_4OH (α=90.0(1)° from single crystal data [34], and 90.088(3)° from powder data [16]), precluded immediate *a priori* identification of the unique axis. Although re-integration of the intensities by sequential release of the constraints on each of the three axes favored the *c*-axis (~21 e.s.d.) over the other two, the refinement with $\gamma \neq 90°$ in that particular case was not successful. The *b*-axis of the orthorhombic lattice-emulating monoclinic cell was identified as the unique axis instead, with β=90.0012(15)°. Despite the low R_{int} factor (2.94%), the initial refinement of the structure on 726 unique reflections resulted in high residuals (R_1=7.03%, $R_{(all\ data)}$=7.08%) indicating twinning. Introduction of a secondary component [1 0 0, 0 −1 0, 0 0 −1] improved the refinement significantly and resulted in R_1 value of 3.11%. The occupancy of the secondary lattice converged to 45%. The position of the hydrogen atom was extracted from the difference electron density around the hydroxyl oxygen. The structure was refined without constraints with SHELXL [35], with isotropic displacement parameters assigned to all atoms. The final parameters at 120 K are: a=8.0545(8) Å, b=8.3622(9) Å, c=5.8755(6) Å, β=90.0012(15), $\alpha=\gamma=90°$, V=395.73(7) $Å^3$, Z=4, ρ_{calc}=4.012 g cm^{-3}, μ=11.051 mm^{-1}, $F(0\,0\,0)$=456. The results are summarized in Tables 2–4.

Similar to Cu_2AsO_4OH [16,34], we found a significant difference in the monoclinic angle of Cu_2PO_4OH for the single-crystal data (β=90.0012(15)°) and synchrotron X-ray powder diffraction

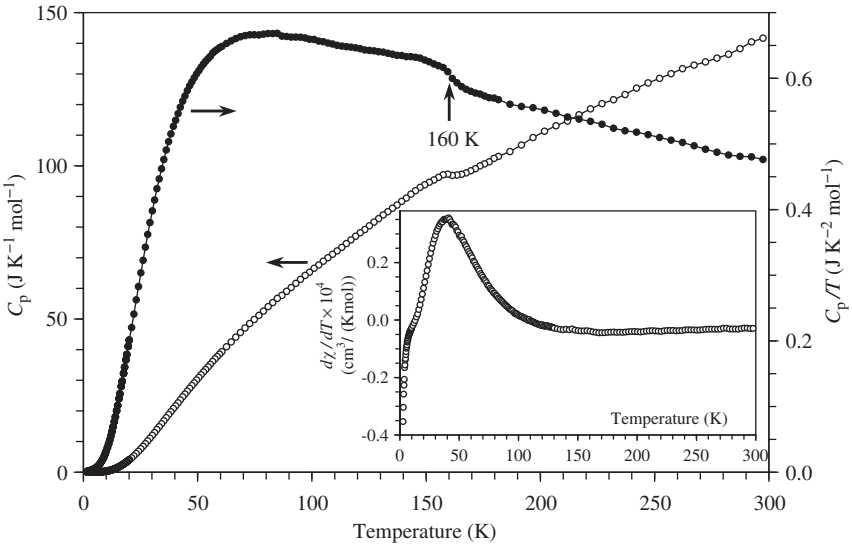

Fig. 4. C_p vs T and C_p/T vs T curves of Cu_2PO_4OH between 1.8 and 300 K measured at a zero magnetic field. The arrow is attached to the anomaly at 160 K. The inset shows the ZFC $d\chi/dT$ vs T curve measured at 1 kOe.

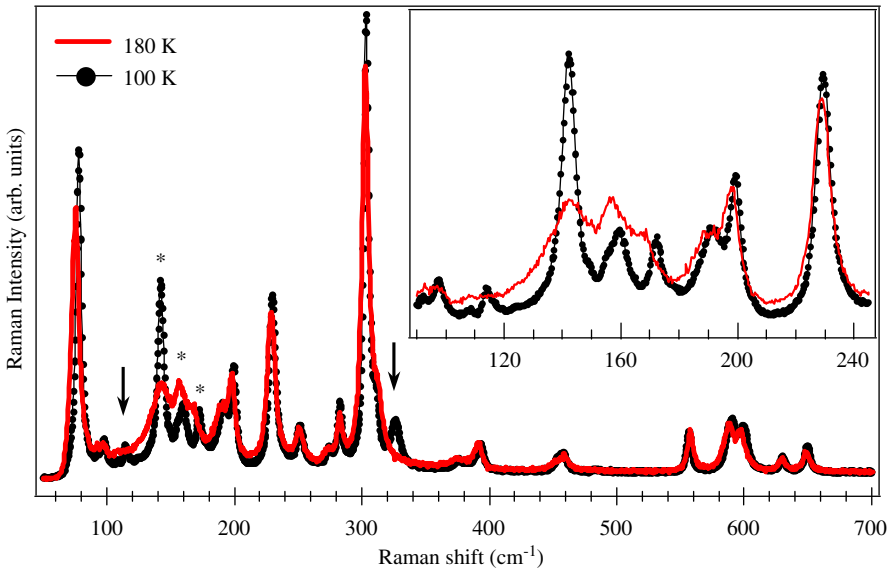

Fig. 5. Raman spectra of Cu_2PO_4OH at 100 K and 180 K between 50 and 700 cm^{-1}. The arrows show new phonon modes that appeared at 100 K. The asterisks show sharpened modes at 100 K. The inset gives an enlarged fragment.

Table 2
Crystallographic and refinement details for libethenite at 180 K and at 120 K.

Temperature	180 K	120 K
Formula weight	239.06	239.06
Wavelength (Å)	0.71073	0.71073
Crystal system	Orthorhombic	Monoclinic
Space group	*Pnnm*	$P2_1/n$
Unit cell dimensions	a=8.0553(8) Å	a=8.0545(8) Å
	b=8.3750(9) Å	b=8.3622(9) Å
	c=5.8818(6) Å	c=5.8755(6) Å
	α=90°	α=90°
	β=90°	β=90.0012(15)°
	γ=90°	γ=90°
Volume (Å^3)	396.80(7)	395.73(7)
Z	4	4
ρ_{calc} (Mg m^{-3})	4.002	4.012
μ (mm^{-1})	11.021	11.051
F(000)	456	456

Table 2 (*continued*)

Temperature	180 K	120 K
Crystal size (mm^3)	$0.20 \times 0.18 \times 0.17$	$0.20 \times 0.18 \times 0.17$
θ (deg.)	3.51–26.23	2.44–26.25
Index ranges	$-9 \leftarrow h \leftarrow 9$ $-9 \leftarrow k \leftarrow 10$ $-7 \leftarrow l \leftarrow 6$	$-9 \leftarrow h \leftarrow 9$ $-10 \leftarrow k \leftarrow 9$ $-6 \leftarrow l \leftarrow 7$
Reflections collected	2702	2925
Independent reflections	419 [$R_{int}=0.0250$]	726 [$R_{int}=0.0294$]
Absorption correction	Empirical	Empirical
Max. and min. transmission	0.2486 and 0.2166	0.2479 and 0.2160
Refinement method	FMLS on F_o^2	FMLS on F_o^2
Data/restraints/parameters	419/0/48	726/0/38
Goodness-of-fit on F_o^2	1.384	1.173
Final R indices [$I>2\sigma(I)$]	$R_1=0.0273$, $wR_2=0.0729$	$R_1=0.0311$, $wR_2=0.0790$
R indices (all data)	$R_1=0.0276$, $wR_2=0.0732$	$R_1=0.0316$, $wR_2=0.0793$
Largest diff. peak and hole/(e $Å^{-3}$)	0.700/−1.707	1.258/−1.619

Table 3
Fractional atomic coordinates and atomic displacement parameters (equivalent for non-hydrogen atoms, and isotropic for the hydrogen atom) of libethenite at 180 K and 120 K.

Atom	x	y	z	U ($Å^2$)
High-temperature phase, 180 K, refined in *Pnnm*				
Cu1	0	0.5	0.24909(9)	0.0053(3)
Cu2	−0.36188(7)	0.37494(7)	0.5	0.0067(3)
P	−0.23315(15)	0.25163(14)	0	0.0034(3)
O1	−0.1338(4)	0.4118(4)	0	0.0044(7)
O2	−0.3417(3)	0.2390(3)	0.2112(4)	0.0087(6)
O3	−0.1021(5)	0.1160(4)	0	0.0131(9)
O4	−0.1239(4)	0.3977(5)	0.5	0.0049(8)
H	−0.094(8)	0.314(8)	0.5	0.001(16)
Low-temperature phase, 120 K, refined in $P2_1/n$				
Cu1	1.00044(18)	0.49997(11)	0.24924(11)	0.0041(2)
Cu2	0.63811(8)	0.37513(8)	0.51307(16)	0.0047(2)
P	0.76695(16)	0.25124(15)	0.0061(3)	0.0031(3)
O1	0.8662(4)	0.4109(4)	0.0013(9)	0.0033(7)
O2	0.6490(7)	0.2463(5)	0.2074(8)	0.0067(11)
O3	0.8969(5)	0.1153(4)	0.0289(8)	0.0052(9)
O4	0.8764(4)	0.3969(4)	0.4979(10)	0.0027(7)
O21	0.6688(7)	0.2308(5)	−0.2158(7)	0.0043(10)
H	0.917(9)	0.297(8)	0.483(15)	0.011(17)

data ($\beta=90.083(1)^\circ$). The difference can be attributed to twinning of the single crystals below the phase transition temperature of 160 K. It should be emphasized that no twinning was observed at 180 K. Therefore, the twinning is a result of slight distortions at low temperatures. The structural distortion is very small. Therefore, a magnetic spin-lattice model is hardly affected and remains very close to a weakly interacting square-spin cluster model with one exchange constant J [27,29]. Indeed, no anomalies were observed in the magnetic susceptibilities at 160 K. On the other hand, for the interpretation of magnetic excitations and inelastic neutron diffraction data the consideration of two non-equivalent exchange constants, J_1 and J_2, may be necessary.

In conclusion, we demonstrated that Cu_2PO_4OH shows a structural phase transition from the low-temperature $P2_1/n$ phase to a high-temperature *Pnnm* phase at 160 K without any additional transitions above room temperature [11]. Cu_2AsO_4OH is monoclinic at room temperature and, therefore, one might expect a high-temperature phase transition to a *Pnnm* phase. The $P2_1/n$–to–*Pnnm* transition may be a general feature of the adamite-type compounds, M_2XO_4OH. Taking into account the fact that this transition has been overlooked in Cu_2PO_4OH in the past, a re-investigation of the low-temperature structural properties of the other members may be a worthwhile exercise.

Table 4
Selected bond lengths in Cu_2PO_4OH at 180 K and 120 K.

180 K		120 K	
Bond[a]	Distance (Å)	Bond[b]	Distance (Å)
Cu1–O1	1.963(2)	Cu1–O1	1.961(5)
Cu1–O1#1	1.963(2)	Cu1–O4	1.968(5)
Cu1–O4#2	1.977(2)	Cu1–O1#1	1.969(5)
Cu1–O4	1.977(2)	Cu1–O4#2	1.984(5)
Cu1–O2#3	2.385(2)	Cu1–O21#3	2.367(5)
Cu1–O2#4	2.385(2)	Cu1–O2#4	2.399(5)
Cu1–Cu1#1	2.9302(11)	Cu1–Cu1#1	2.9288(13)
Cu1–Cu1#2	2.9516(11)	Cu1–Cu1#2	2.9467(13)
Cu2–O4	1.926(4)	Cu2–O4	1.930(4)
Cu2–O3#5	1.937(4)	Cu2–O3#5	1.946(4)
Cu2–O3#4	2.039(4)	Cu2–O21#6	2.014(5)
Cu2–O2	2.051(3)	Cu2–O3#4	2.043(4)
Cu2–O2#6	2.051(3)	Cu2–O2	2.096(5)
Cu2–Cu2#7	3.0560(12)	Cu2–Cu2#7	3.0553(13)
P–O2#8	1.523(3)	P–O2	1.518(5)
P–O2	1.523(3)	P–O21	1.534(5)
P–O3	1.551(4)	P–O3	1.551(4)
P–O1	1.562(4)	P–O1	1.556(4)
O4–H	0.74[c]	O4–H	0.97[c]

[a] Symmetry codes: #1 $-x$, $-y+1$, $-z$; #2 $-x$, $-y+1$, $-z+1$; #3 $x+1/2$, $-y+1/2$, $-z+1/2$; #4 $-x-1/2$, $y+1/2$, $-z+1/2$; #5 $x-1/2$, $-y+1/2$, $z+1/2$; #6 x, y, $-z+1$; #7 $-x-1$, $-y+1$, $-z+1$; #8 x, y, $-z$.
[b] Symmetry codes: #1 $-x+2$, $-y+1$, $-z$; #2 $-x+2$, $-y+1$, $-z+1$; #3 $x+1/2$, $-y+1/2$, $z+1/2$; #4 $-x+3/2$, $y+1/2$, $-z+1/2$; #5 $x-1/2$, $-y+1/2$, $z+1/2$; #6 x, y, $z+1$; #7 $-x+1$, $-y+1$, $-z+1$.
[c] Refined without constraints.

Acknowledgments

This work was supported by World Premier International Research Center Initiative (WPI Initiative, MEXT, Japan), the NIMS Individual-Type Competitive Research Grant, the Japan Society for the Promotion of Science (JSPS) through its "Funding Program for World-Leading Innovative R&D on Science and Technology (FIRST Program)", the Grants-in-Aid for Scientific Research (22246083) from JSPS, Japan and partially also by a Global COE program, "The Global Education and Research Center for Bio-Environmental Chemistry" from the Ministry of Education, Culture, Sports, Science and Technology, Japan. The synchrotron radiation experiments were performed at the SPring-8 with the approval of the Japan Synchrotron Radiation Research Institute (Proposal Numbers: 2007A2087 and 2009A1136). A part of this research was supported by NIMS hub-center of "Low-Carbon Research Network" funded by the Ministry of Education, Culture, Sports,

Science and Technology (MEXT), Japan. We would like to thank Dr. Kenji Watanabe in NIMS for his support with the Raman measurements.

Appendix A. Supplementary materials

Supplementary data associated with this article can be found in the online version at doi:10.1016/j.jssc.2011.09.026.

References

[1] 〈http://euromin.w3sites.net/mineraux/LIBETHENITE.html〉.
[2] 〈http://www.mindat.org/min-2394.html〉.
[3] I.S. Cho, D.W. Kim, S. Lee, C.H. Kwak, S.T. Bae, J.H. Noh, S.H. Yoon, H.S. Jung, D.W. Kim, K.S. Hong, Adv. Funct. Mater. 18 (2008) 2154.
[4] C.H. Kwak, I.S. Cho, S. Lee, J.S. An, K.S. Hong, J. Nanosci. Nanotech. 10 (2010) 1185.
[5] F.S. Xiao, J.M. Sun, X.J. Meng, R.B. Yu, H.M. Yuan, J.N. Xu, T.Y. Song, D.Z. Jiang, R.R. Xu, J. Catal. 199 (2001) 273.
[6] X.J. Meng, K.F. Lin, X.Y. Yang, Z.H. Sun, D.Z. Jiang, F.S. Xiao, J. Catal. 218 (2003) 460.
[7] J. Xu, D. Xue, J. Phys. Chem. B 110 (2006) 7750.
[8] O.V. Yakubovich, O.K. Melnikov, Kristallografiya 38 (1993) 63.
[9] A. Cordsen, Can. Miner. 16 (1978) 153.
[10] P. Keller, H. Hess, F. Zettler, Neues Jahrb. Mineral.-Abh. 134 (1979) 147.
[11] M. Zema, S.C. Tarantino, A.M. Callegari, Mineral. Mag. 74 (2010) 553.
[12] N.C.G. Reddy, R.R. Reddy, G.S. Reddy, S.L. Reddy, B.J. Reddy, Cryst. Res. Technol. 41 (2006) 400.
[13] W. Martens, R.L. Frost, Am. Miner. 88 (2003) 37.
[14] R.L. Frost, P.A. Williams, W. Martens, J.T. Kloprogge, P. Leverett, J. Raman Spectrosc. 33 (2002) 260.
[15] R.S.W. Braithwaite, R.G. Pritchard, W.H. Paar, R.A.D. Pattrick, Mineral. Mag. 69 (2005) 145.
[16] P.C. Burns, F.C. Hawthorne, Can. Mineral. 33 (1995) 885.
[17] J.M. Rojo, J.L. Mesa, L. Lezama, J.L. Pizarro, M.I. Arriortua, J.R. Fernandez, G.E. Barberis, T. Rojo, Phys. Rev. B 66 (2002) 094406.
[18] I. de Pedro, J.M. Rojo, J.R. Fernandez, M.T. Fernandez-Diaz, T. Rojo, Phys. Rev. B 81 (2010) 134431.
[19] J.M. Rojo, J.L. Mesa, L. Lezama, G.E. Barberis, T. Rojo, J. Magn. Magn. Mater. 157–158 (1996) 493.
[20] I. de Pedro, J.M. Rojo, V. Jubera, J.R. Fernandez, J.S. Marcos, L. Lezama, T. Rojo, J. Mater. Chem. 14 (2004) 1157.
[21] I. de Pedro, J.M. Rojo, J.L. Pizarro, J.R. Fernandez, J.S. Marcos, M.T. Fernandez-Diaz, M. Arriortua, T. Rojo, J. Mater. Chem. 17 (2007) 3915.
[22] I. de Pedro, V. Jubera, J.M. Rojo, L. Lezama, J. Sanchez Marcos, J. Rodríguez Fernández, J.L. Mesa, T. Rojo, M.I. Arriortua, J. Magn. Magn. Mater. 272–276 (2004) E665.
[23] I. de Pedro, J.M. Rojo, J.L. Pizarro, J.R. Fernandez, J.S. Marcos, M.T. Fernandez-Diaz, M.I. Arriortua, T. Rojo, J. Phys.: Condens. Matter 18 (2006) 3767.
[24] I. de Pedro, J.M. Rojo, J.R. Fernandez, L. Lezama, T. Rojo, Eur. J. Inorg. Chem. 17 (2010) 2514.
[25] V.N. Viter, Phosphorus Sulfur Silicon Relat. Elem. 185 (2010) 602.
[26] I. de Pedro, J.M. Rojo, J.L. Pizarro, J. Rodríguez Fernández, M.I. Arriortua, T. Rojo, J. Solid State Chem. 184 (2011) 2075.
[27] A.A. Belik, H.-J. Koo, M.-H. Whangbo, N. Tsujii, P. Naumov, E. Takayama-Muromachi, Inorg. Chem. 46 (2007) 8684.
[28] C.N. Kuo, C.S. Lue, Phys. Rev. B 78 (2008) 212407.
[29] T. Asai, H. Saheki, R. Kiriyama, Bull. Chem. Soc. Jpn. 52 (1979) 310.
[30] E. Nishibori, M. Takata, K. Kato, M. Sakata, Y. Kubota, S. Aoyagi, Y. Kuroiwa, M. Yamakata, N. Ikeda, Nucl. Instrum., Methods Phys. Res. Sect. A 467–468 (2001) 1045.
[31] F. Izumi, T. Ikeda, Mater. Sci. Forum 321–324 (2000) 198.
[32] Bruker A.X.S. Inc. SMART-NT, SAINT-Plus-NT and SADABS. Madison, Wisconsin, USA, 1996.
[33] 5th ed.,T. Hahn (Ed.), International Tables for Crystallography, vol. A, Kluwer, Dordrecht, The Netherlands, 2002, p. 52.
[34] K. Toman, Acta Crystallogr. B33 (1977) 2628.
[35] G.M. Sheldrick, SHELXL-97. Structure refinement program. University of Göttingen, Germany, 1997.